Journal of the Korean Society of Remote Sensing, Vol.15, No.2, 1999, pp.131~146

Simulation and Evaluation of the KOMPSAT/OSMI Radiance Imagery

Delu Pan* and Yong-Seung Kim**

Second Institute of Oceanography, State Oceanic Administration, PRC*
Satellite Division, Korea Aerospace Research Institute**

다목적 실용위성 해색센서 (OSMI)의 복사영상에 대한 모의 및 평가

반덕로* · 김용승**

중국국가해양국 제2해양연구소*, 한국항공우주연구소 위성사업부**

Abstract : The satellite visible data have been successfully applied to study the ocean color. Another ocean color sensor, the Ocean Scanning Multi-spectral Imager (OSMI) on the Korea Multi-Purpose Satellite (KOMPSAT) will be launched in 1999. In order to understand the characteristics of future OSMI images, we have first discussed the simulation models and procedures in detail, and produced typical patterns of radiances at visible bands by using radiative transfer models. The various simulated images of full satellite passes and Korean local areas for different seasons, water types, and the satellite crossing equator time (CET) are presented to illustrate the distribution of each component of radiance (i.e., aerosol scattering, Rayleigh scattering, sun glitter, water-leaving radiance, and total radiance). A method to evaluate the image quality and availability is then developed by using the characteristics of image defined as the Complex Signal Noise Ratio (CSNR). Meanwhile, a series of CSNR images are generated from the simulated radiance components for different cases, which can be used to evaluate the quality and availability of OSMI images before the KOMPSAT will be placed in orbit. Finally, the quality and availability of OSMI images are quantitatively analyzed by the simulated CSNR image. It is hoped that the results would be useful to all scientists who are in charge of OSMI mission and to those who plan to use the data from OSMI.

Key Words : Radiance, CSNR, Simulation, Image Quality

요 약 : 가시광선 위성자료는 해색 연구에 성공적으로 응용되어 왔다. 또 하나의 해색관측 센서인 OSMI가 다목적 실용위성에 탑재되어 1999년 발사될 예정이다. 향후 OSMI 영상특성을 이해하기 위해서 우선 모의실험 절차를 자세히 논의하고 복사전달 모델을 이용하여 전형적인 경우의 가시대역 복사패턴을 모의 생성시켰다. 각 성분의 복사량 (에어로졸 산란, Rayleigh 산란, 태양복사, 해수 상향 복사량 및 총 복사량) 분포를 설명하기 위해 계절별, 해수형태 및 위성의 적도 통과 시각에 대한

Received 25 March 1999 ; Accepted 7 May 1999.

위성의 전체 통과 경로와 한국 근해지역의 여러 가지 모의 영상들이 소개된다. 그리고 영상의 품질 및 가용도를 평가하기 위한 방법은 복합신호잡음비 (CSNR)로 정의된 영상특성을 이용해 개발된다. 한편, 다목적 실용위성이 궤도에 진입 되기 전에 OSMI 영상자료의 질과 가용도를 평가할 수 있도록 일련의 CSNR영상이 서로 다른 경우에 대한 모의 복사량 성분들로부터 생성된다. 최종적으로 OSMI 영상의 질과 가용도가 CSNR모의 영상을 이용해 정량적으로 분석된다. 본 연구결과가 OSMI 임무를 책임지고 있는 모든 과학자들과 OSMI 자료활용을 계획하고 있는 사람들에게 유용하게 되기를 기대한다.

1. Introduction

In any successful program of space satellite remote sensing in the world such as meteorology, oceanography and land satellites, more attention is paid to the simulation of radiance imagery, before the satellite will be in orbit. The radiance imagery can be simulated with the designed properties of orbit, sensor, and certain cases of atmosphere and water, by using the models of geometric calculation of sun-water-sensor and the models of radiative transfer in the atmosphere, air/water, and subsurface water. The simulated data have been successfully used to decide the requirements of satellite orbit and sensor properties and to validate their appropriateness during the design phase, based on the analysis of the future satellite data quality and availability. And the simulated data allow users to prepare data analysis such as algorithm development and software testing before actual satellite data are downlinked to the ground station.

The optical properties of seawater, generally termed as ocean color, are determined by the water itself and its contents (Hooker *et al.*, 1992). The ocean color can be retrieved from the water leaving radiance that is part of the spaceborne sensor measurements. The water leaving radiance will be modified by the scattering and absorption of the atmosphere and by the geometric parameters such as the solar and sensor zenith and azimuth angles. Actually, over oceans, most part (more than 85%) of the total radiance arrived at sensor are contributed by atmospheric radiation and sun glitter which depends on the satellite orbit and sensor geometry (Bricaud and Morel, 1987, Andre and Morel, 1989, Hooker *et al.*, 1992). The OSMI is designed to detect and map the sea water contents, such as phytoplankton suspended material and yellow substance. Because of no tilt capability of OSMI, the atmospheric radiance and sun glitter may be critical to the success of OSMI mission. Before placing the satellite in orbit, it is important to assess how OSMI imagery look like and how sun glitter, the atmospheric and sea conditions, the Crossing Equator Time (CET), and the time of the year will affect them.

2. Simulation Models and Procedures

In the optical transmission system of ocean color remote sensing, sun-atmosphere-air/water-water-sensor, the transfer of solar radiation is generally separated into two parts. One part is scattered backward directly to the sensor of the satellite. The other part is scattered forward to arrive at the water surface by which one part is reflected and the other part is refracted into water and scattered and absorbed by particles (e.g.,

chlorophyll, suspended material, and yellow substance). Under water, the part of radiance, i.e., water- leaving radiance that contains the signal of water property, is scattered upward and reaches to the sensor via atmosphere. Therefore, the total radiance captured by the sensor can be split into four components as follows (Gordon, 1990).

$$L_t(\lambda) = L_r(\lambda)+L_a(\lambda)+L_{sr}(\lambda)+L_w(\lambda) \qquad (1)$$

where $L_t(\lambda)$ is the total radiance received by the sensor, $L_r(\lambda)$ is the Rayleigh radiance, $L_a(\lambda)$ is the aerosol radiance, $L_{sr}(\lambda)$ is the specularly reflected solar (including sky component) radiance (sun glitter) which can be calculated (Sturm, 1981) from the wave slope distribution as a function of the wind speed (Cox and Munk, 1954), and $L_w(\lambda)$ is the water-leaving radiance. Each component of radiance for any given pixel can be simulated for different cases, by means of geolocation and radiative transfer models.

1) Geolocation

All components in Eq. (1) are functions of the solar and sensor zenith and azimuth angles. Therefore, we need to determine the geolocation of given pixels (i.e., defining the latitude and longitude of each pixel in the simulation image).

The satellite flies around the earth in its orbit. The sensor scans and images the ocean surface by a rotating scan mirror. The relationship between the geographic and the image coordinates is a function of the satellite flight direction and the scanning direction of sensor. The two-dimensional movement of sensor is the flight direction along the orbit corresponding to the line number of image and the scanning direction across the orbit corresponding to the pixel number in the scanning line. Meanwhile, the two-dimensional movement of sensor is not a simple scanning on a static plane surface, but relative to the spherical earth surface, which rotates around its polar axis. In principle, if the geographic coordinates of one pixel in the image are known, it is possible to calculate the geographic coordinates of other pixels by using the satellite orbit parameters and sensor properties. The satellite orbit and sensor parameters include the satellite altitude (km), flight direction (descending or ascending), inclination angle (degrees), date (in Julian day), crossing equator time (CET), orbit period (min), the field of view (FOV), scanning rate (line/ second), and total number of pixels per scanning line. With the coordinate transformation, the latitude and longitude (GB, GL), the solar and sensor zeniths (θ_s, θ_v) and the azimuth between the sun and sensor (φ) (sun's-nadir-pixel-sensor's nadir) are calculated for each pixel of the image.

In the model, the earth's curvature and rotation, the motion of the satellite relative to the pixel on earth surface, and different cases of orbital inclination are considered. Assuming the crossing equator point to be the center of the simulated image (GM_m, GL_m), the geographic coordinates (GB, GL) of each pixel can be calculated by the following coordinate transformation (Pan *et al.*, 1996) :

(1) Calculate the earth spherical coordinates (X, Y) corresponding to the image coordinates (I_x, I_y).
(2) Derive the central polar coordinates (R, S) corresponding to (X, Y).
(3) Compute the arctic polar coordinates (U, V) from (R, S).
(4) Transform (U, V) into the geographic coordinates (GB, GL).
(5) Finally, the solar and sensor zenith angles (θ_s, θ_v), and the azimuth angle (φ) of the sun -pixel -scanner can be calculated from (GB, GL).

2) Atmospheric Transmittance

The direct transmittance (t_d) depends on the

following five components (Iqbal, 1983):

$$t_d = t_r t_a t_{oz} t_{mg} t_{wv} \quad (2)$$

wheret t_r t_a, t_{oz}, t_{mg} and t_{wv} are the trasmittances of Rayleigh, aerosol, ozone, mixed gas (such as CO_2, and O_2,), and water vapor, respectively. They can be calculated by the following equations (Iqbal, 1983). Rayleigh transmittance (t_r) is given by

$$t_r = \exp(-0.008735\ \beta\lambda^{-4.08}\ m_a) \quad (3)$$

where λ is wavelength, β is the volume scattering function [see Eq. (6)], and m_a is the atmospheric optical mass as:

$$m_a = [\cos\theta_z + 0.15(93.885 - \theta_z)^{-1.253}]^{-1} \cdot (p/1013.25) \quad (4)$$

where p is the air pressure (hPa) and θ_z is the viewing zenith angle. Aerosol transmittance (t_a) is as follows:

$$t_a = \exp(-\beta\lambda^{-2} m_a) \quad (5)$$

When the optical horizontal visibility is more than 5km, β can be calculated from the following equation:

$$\beta = (0.55)^{\alpha}\ (3.912/vis - 0.01162)[0.02422\ (vis-5)+1.132] \quad (6)$$

where α could be between 0.5 and 2.5 (normally α=1.3 for most case of air vis and is horizontal visibility (km). Ozone transmittance (t_{oz}) is determined by:

$$t_{oz} = \exp(-K_{0\lambda}\ A_{oz}\ m_0) \quad (7)$$

where $K_{0\lambda}$ is the attenuation coefficient of ozone at a given wavelength λ, A_{OZ} is the total amount of ozone [cm (NTP)], and m_0 is the optical mass as:

$$m_0 = \frac{1.0035}{\cos^2\theta_z + 0.007^{-0.5}} \quad (8)$$

Transmittance for mixed gas (t_{mg}) is as follows:

$$t_{mg} = \exp[-1.41 K_{g\lambda} m_a / (1+118.93 K_{g\lambda} m_a)^{0.45}] \quad (9)$$

where $K_{g\lambda}$ is the attenuation coefficient of mixed gas. Water vapor transmittance (t_{wv}) is calculated by

$$t_{wv} = \exp[-0.2385 K_{w\lambda} \cdot W \cdot m_w / (1+20.07 K_{w\lambda} \cdot W \cdot m_w)^{0.45}] \quad (10)$$

where $K_{w\lambda}$ is the attenuation coefficient of water vapor, W is the precipitable water m_w(cm), and is the optical mass of water vapor given by

$$m_w = [\cos\theta_z + 0.0548(92.65 - \theta_z)^{-1.452}]^{-1} \quad (11)$$

In the above equations (2) through (11), the transmittance of the direct solar component through the air has been described. In addition to the direct component, some of the scattered Rayleigh and aerosol radiance has to be considered. Then, the total transmittance is as follows:

$$t = t_d + t_s \quad (12)$$

where t_d is the transmittance of the direct component from Eq. (2) and t_s is the trasmittance of the diffuse component:

$$t_s = t_{aa} t_{oz} t_{mg} t_{wv} [\frac{1-t_r^{0.95}}{2} + t_r^{1.5}\ F_a(1-t_{as})] \quad (13)$$

where F_a is the forward scattering coefficient of aerosol, t_{aa} is the aerosol trasmittance after absorption

$$t_{aa} = \exp[-(1-\omega_a)\tau_a m_a] \quad (14)$$

and t_{as} is the transmittance after scattering

$$t_{as} = \exp(-\omega_a \tau_a m_a) \quad (15)$$

where ω_a is the single scattering albedo, τ_a is the optical mass of aerosol which is $\beta\lambda^{-2}$ in Eq. (5). The above transmittances are the function of θ_x. For example, when $\theta_x = \theta_s$ $t_x(\theta_s)$ is the downward transmittance for any given component of radiance.

3) Atmospheric Path Radiance

The path radiance includes Rayleigh and aerosol scattering. Not only the single scattering arriving at sensor but also the specula reflection from the water surface are considered in both calculation of Rayleigh and aerosol scattering (Gordon and Castano, 1989):

$$L_x = F_s \tau_x \omega_x p_x(\theta_v, \theta_s)/(4\pi \cos\theta_v) \quad (16)$$

where L_x is the radiance of Rayleigh or aerosol scattering; L_x is Rayleigh scattering when x = r and L_x is the aerosol scattering when x = a. F_s is the instantaneous extraterrestrial solar irradiance and calculated by

$$F_s = F_0(\lambda)\,[1+0.0167\cos\frac{2\pi(D-3)}{365}]^2 \quad (17)$$

where $F_0(\lambda)$ is the mean extraterrestrial solar irradiance and D is the Julian day.
ω_x is the single scattering albedo and P_x is the scattering phase function and calculated by

$$P_x(\theta_v, \theta_s) = P_x(\theta^-)+[\rho(\theta_v)+\rho(\theta_s)]P_x(\theta^+) \quad (18)$$

where $P_x(\theta^-)$ and $P_x(\theta^+)$ are the backward and forward scattering phase functions, respectively. And ρ is the Fresnel reflectance for solar (θ_s) and viewing (θ_v) geometries, respectively. The aerosol scattering phase function $P_a(\theta^\pm)$ can be calculated by the following Henyey-Greenstein function:

$$P_a(\theta^\pm) = \frac{\alpha(1-g_1^2)}{(1+g_1^2-2g_1\cos\theta^\pm)^{1.5}} + \frac{(1-\alpha)(1-g_2^2)}{(1+g_2^2-2g_2\cos\theta^\pm)^{1.5}} \quad (19)$$

where $\alpha = 0.983$, $g_1 = 0.82$, $g_2 = -0.55$, and

$$\cos\theta^\pm = \pm\cos\theta_v\cos\theta_s - \sin\theta_v\sin\theta_s\cos(\varphi) \quad (20)$$

The specula reflectance $\rho(i)$ is as follows:

$$\rho(i) = 0.5[\sin^2(i-j)/\sin^2(i+j)+\tan^2(i-j)/\tan^2(i+j)] \quad (21)$$

where i represents the incident zenith angles (θ_s or θ_v), j is the refracted zenith and can be calculated by Snell's law.

$$j = \sin^{-1}[\sin(i)/n] \quad (22)$$

where n is the water refractive index and taken to be 4/3.

4) Sun Glitter

The specula reflectance of direct sun light at a rough sea surface can be calculated based on the formula for calculating the distribution of wave slopes as a function of the wind-speed. With the two ways of diffuse trasmittance through the atmosphere, the sun glitter radiance arrived at the sensor may be written as (Sturm, 1981, Cox and Munk, 1954):

$$L_{sr} = F_s t_d(\theta_s) \cdot t_u(\theta_v) g \cos\theta_s \quad (23)$$

g is the coefficient of reflectance of sun glitter as follows:

$$g = [\rho(\omega)\cos\omega/(\cos\theta_v\cos\theta_s)]/\exp[(-\tan^2\beta/\sigma^2)/(4\pi\sigma^2\cos^4\beta)] \quad (24)$$

where $\sigma = 0.003 + 0.00512V_w$ (25)

$$\omega = 0.5\cos^{-1}[\cos\theta_v\cos\theta_s - \sin\theta_v\sin\theta_s\cos\varphi] \quad (26)$$

$$\beta = \cos^{-1}[(\cos\theta_v+\cos\theta_s)/(2\cos\omega)] \quad (27)$$

and V_w is the wind speed.

5) Water Leaving Radiance

The solar radiation arrived at the water surface is refracted into subsurface. This part of radiation is scattered back to the sensor by the water substance such as plankton, suspended material and water (Fischer, 1983). One part of the

refracted radiation in the subsurface is absorbed by the phytoplankton and is converted to the fluorescence with the photosynthesis, and is subsequently transmitted to the sensor. Thus the total water leaving radiance can be written as follows:

$$L_w = L_{ws} + L_{wf} \tag{28}$$

where L_w, L_{ws} and L_{wf} are the total, visible, and fluorescence water leaving radiance, respectively. The solar irradiance refracted into the subsurface through the air/water interface is:

$$E_{wd} = F_s t_d(\theta_s) T_d(\theta_s) \tag{29}$$

where E_{wd} is the solar irradiance at the subsurface, $t_d(\theta_s)$ is the total downward transmittance of atmosphere, and $T_d(\theta_s)$ is the transmittance from air to water subsurface and can be calculated by:

$$T_d(\theta_s) = (1-\rho_a)\cos\theta_s \tag{30}$$

where ρ_a is the average specula reflectance of different directions, normally equals 0.06. The water leaving radiance reflected through the water/air interface can be calculated as follows:

$$L_{ws} = [E_{wd} \cdot R \cdot T_u(\theta_v) \cdot t_u(\theta_v)]/Q \tag{31}$$

where R is the irradiance reflectance of water surface, Q is the factor of the conversion from irradiance to radiance and normally equals 4.5, $t_u(\theta_v)$ is the total upward transmittance of atmosphere, $T_u(\theta_v)$ is the transmittance of water/air and can be calculated by:

$$T_u(\theta_v) = [1-\rho(\theta_v)]/n^2 \tag{32}$$

where n is the refractive index of water and normally equals 1.33. The irradiance reflectance of water surface can be computed by two stream models as follows:

$$R=(K_t-a_t)/(K_t+a_t) \tag{33}$$

where K_t and a_t are the coefficients of the scattering and the absorption of the subsurface water (Pan *et al.*, 1997), which depend on the water constituents, e.g., chlorophyll, suspended material and yellow substance. The a_t and K_t are calculated as:

$$a_t = a_w + C_c a_c + C_s a_s + C_g a_g \tag{34}$$

$$K_t = K_w + C_c K_c + C_s K_s + C_g K_g \tag{35}$$

In the above, a_w and K_w are the coefficients of absorption and scattering of pure water. (a_c, a_s, a_g) and (K_c, K_s, K_g) are the coefficients of absorption and scattering per unit of chlorophyll, suspended material and yellow substance. The units of a_c, a_g, K_c and K_g are in m^2/mg and K_s are in m^2/g. C_c, C_s, C_g are the concentrations of chlorophyll, suspended material and yellow substance, respectively. The units of C_c and C_g are in $mg \cdot m^{-3}$ and C_s in $g \cdot m^{-3}$.

To calculate the contribution by the stimulated chlorophyll fluorescence to the upwelling irradiance, the following procedure can be used as an approximation (Doerffer, 1980):

The total solar radiation in the wavelength range $\lambda_1 - \lambda_2$ absorbed by the phytoplankton pigment is

$$E_{af} = \int_{\lambda_1}^{\lambda_2} E_d[1-R(\lambda)] \frac{C_c a_c(\lambda)}{a_t(\lambda)} d\lambda \tag{36}$$

where $\lambda_1 = 0.4\mu m$, $\lambda_2 = 0.675\mu m$.

The emitted energy into the upper hemisphere E_{uf} is

$$E_{uf} = 0.5\, E_{af} F_{ef} \tag{37}$$

where F_{ef} is fluorescence efficiency and normally is 0.003. Since the fluorescence energy is emitted over a broad band which can be described by a Gaussian shape with a standard deviation of λ =10.6 nm, equivalent to a half band width of 25 nm, the fluorescence energy has to be distributed over a wavelength band for each wavelength, λ_f, around the wavelength of maximum fluorescence

energy (λ_0 =0.685μm assumed).

The weight $g(\lambda_f)$ for the wavelength interval $d\lambda$ is calculated by

$$g(\lambda_f) = (2\pi\lambda^2)^{-1/2} \exp[\frac{-(\lambda_f-\lambda_0)^2}{2\lambda^2}] \quad (38)$$

The effect that the mean penetration depth for the absorbed solar radiation is different from the mean depth from which the fluorescence energy arrives at the surface (due to the different attenuation in the blue-green and in the red spectra range) can be calculated by the factor for each emission wavelength by using the following procedure.

The mean excitation depth Z_{ex} weighted by the absorption of phytoplankton pigments for the spectral range λ_1–λ_2 is

$$Z_{ex} = \frac{\sum_{\lambda i=1}^{n} C_c a_c(\lambda_i)}{\sum_{\lambda i=1}^{n} K_t(\lambda_i) C_c a_c(\lambda_i)} \quad (39)$$

The total radiance of the fluorescence leaving water surface is

$$F_u(\lambda) = \frac{E_{uf} g(\lambda)}{Z_{ex} \cdot K_t(\lambda)} \quad (40)$$

The radiance of the fluorescence arriving at the sensor is

$$L_{wf} = F_u(\lambda) \cdot T_u(\theta_v) \cdot t_u(\theta_v)/Q \quad (41)$$

where $T_u(\theta_v)$ is the transmittance of the water/air interface.

6) Simulation Procedures

The simulation procedures to generate radiance imagery are as follows:

(1) Geolocation and calculation of geometrical parameters for each pixel of the image.

(2) Calculation of the optical parameters, e.g., atmospheric trasmittance $t_x(\theta_s)$, $t_x(\theta_v)$, and optical thickness τ_x by the atmospheric characteristics such as air pressure (hPa), the amount of the ozone, mixed gas, water vapor [cm (NTP)], precipitation, horizontal visibility, wind speeds.

(3) Computation of the optical parameters of subsurface water such as albedo, the radiance of the fluorescence, and the transmittance of the air/water interface by the water constituents e.g., chlorophyll, suspended material, and the yellow substance.

(4) Derivation of each component of radiances L_r, L_a, L_{sr}, L_w and L_t arriving at the sensor.

(5) Digitization and simulation of the radiance image in the following steps:

(a) Computation of spectral radiance for a given band of sensor as follows:

$$F_x^i = [\int_{\lambda 1}^{\lambda 2} L_x(\lambda) S(\lambda) d\lambda]/(\lambda_1-\lambda_2) \quad (42)$$

where λ_1–λ_2 the wavelength range of the bands, S(λ) is the sensitivity of the band with respect to the wavelength, x is the subscript which represents r, a, sr, w and t respectively corresponding to Rayleigh, aerosol, sun glitter, water leaving, and the total radiance.

(b) The irradiance F_x^i of each band is

$$F_x^i = L_x^i \pi \quad (43)$$

(c) The albedo A_x^i of each band by scaling the extraterrestrial solar irradiance:

$$A_x^i = F_x^i / F_s^i \quad (44)$$

where F_s^i is the extraterrestrial solar irradiance.

(d) Digitization of the radiance of each band by the gain G_x^i and intercept I_x^i of the sensor:

$$D_x^i = (A_x^i - I_x^i)/G_x^i \quad (45)$$

If the gain G_x^i and intercept I_x^i are unknown, then,

$$D_x^i = 2^n A_x^i \quad (46)$$

where n is the digitizing bit.

(6) Generation of Mercator projection of the radiance image based on the results of geolocation calculation.

Based on the above procedures, the individual component of radiance for the OSMI spectral band can be produced and will be discussed in section 5.

3. Evaluation Models and Procedures

1) Evaluation Models

The quality and availability of OSMI images depend not only on the complex radiation transmission system that has been discussed above in detail, but also on the technical level of data processing, such as the accuracy of atmospheric correction. Here, a key index of the image, herein after called complex signal noise ratio (CSNR) is introduced for the evaluation of the image quality index (IQI). CSNR is defined as follows:

$$CSNR = L_w(\lambda)/L_N(\lambda) \tag{47}$$

where $L_w(\lambda)$ is the water leaving radiance calculated by Eq. (28). $L_w(\lambda)$ contains a useful signal to measure the water properties determined by the concentration of phytoplankton, suspended material, and yellow substance. $L_N(\lambda)$ is a complex noise that could be contributed by the following sources:

(1) Remained noise from atmospheric correction

In the raw image, the total sum of $L_a(\lambda)$, $L_r(\lambda)$ and $L_{sr}(\lambda)$ (see the right items of Eq. (1)) is about 85% of the total radiance received by sensor. The atmospheric correction is no doubt necessary for the ocean color retrieval. Since the CZCS data was available in 1978, scientists in the word have made every effort to remove the atmospheric path radiance and sun glitter. But it is not possible to remove all of them so far, and even in the future because of random variations of air properties with the space and time in the large scale of satellite coverage. It means that the remained noise is still involved in the image for which the atmospheric correction has been made. How much the remained noise will be in the pre-processed image? It depends on the data correction accuracy of $L_a(\lambda)$, $L_r(\lambda)$ and $L_{sr}(\lambda)$. Suppose that A, B and C are the calculation accuracy of $L_a(\lambda)$, $L_r(\lambda)$ and $L_{sr}(\lambda)$, respectively, with the error relative to their own totals, then their remained noises are $AL_a(\lambda)$, $BL_r(\lambda)$, and $CL_{sr}(\lambda)$, respectively.

(2) Inherent sensor noise

The sensor sensitivity could normally be characterized by the signal to noise ratio SNR. The inherent sensor noise can be approximately estimated as $L_t(\lambda)$/SNR, where $L_t(\lambda)$ is the total radiance received by the sensor.

(3) Sensor calibration

The requirement of accuracy of radiance measurement for ocean color is normally less than 5%, with the error relative to the total radiance. The sensor calibration accuracy should meet the above requirement. Hence, the sensor calibration error will also contribute the noise for CSNR.

Based on the above analysis of noise sources, the total remained noise $L_N(\lambda)$ in the image can be estimated as follows:

$$L_N(\lambda) = \sqrt{[A^2+D^2La(\lambda)]^2 + [B^2+D^2Lr(\lambda)]^2 + [C^2+D^2Lsr(\lambda)]^2 + [1 + D^2 L(\lambda)/SNR]^2} \tag{48}$$

where A, B and C are the calculation accuracy of $L_a(\lambda)$, $L_r(\lambda)$ and $L_{sr}(\lambda)$, respectively, and D is the sensor calibration accuracy. It is obvious that the higher CSNR of the pixel is the better quality of a pixel in the image. Therefore, CSNR is a reasonable index to evaluate the image quality.

Meanwhile, a threshold of $CSNR_t$ (minimum CSNR) may be used to determine whether or not a given pixel is available. For example, if CSNR of one pixel is less than $CSNR_t$, then the pixel will be judged as an unavailable pixel. As mentioned above, the requirement of radiance measurement accuracy is normally 5% with the error relative to total radiance and thus $CSNR_t$ is chosen to be 20 in this study. Then the availability of whole image is defined as follows:

$$AVA = N_a/N_t \tag{49}$$

where AVA is the availability of whole image, N_a is the number of available pixels determined by Eq. (49), and N_t is the total number of pixels in the image.

2) Evaluation Procedures

The evaluation procedures of CSNR and AVA are as follows:

(1) Calculation of the radiance of different components $L_a(\lambda)$, $L_r(\lambda)$, $L_{sr}(\lambda)$ and $L_w(\lambda)$ for each pixel, with the specification of the satellite orbit and sensor characteristics and the atmosphere and water properties.

(2) Computation of the total remained noise in the image by Eq. (48).

(3) Derivation of CSNR from Eq. (47) as the Image Quality Index to produce the IQI image.

(4) Determination of the pixel to be available or not and finally the availability of whole image by Eq. (49).

4. Parameters in Simulation and Evaluation

The orbit and sensor parameters of OSMI are as follows (Paik *et al.*, 1998):

(1) Obit: 685 km altitude, 10:50 AM (assumed 8:00-16:00 AM) ascending, 98.13 degree inclination and 98.5 min period sun-synchronous.

(2) Sensor: 60 degree FOV, 1044 pixels per each scan line, 6 bands from 8 bands in Table 1, sensor spectral sensitivity S(l) = 1.0. Digitizing 10 bits with gain $G^i = 1.0$, intercept $I^i = 0$.

(3) The parameters of atmosphere, water, and the dates in the simulation are described in Table 2.

5. Discussion and Results

1) Image Properties of Different Bands

The total radiance arrived at OSMI for case I and case II water decreases with the spectral wavelength as shown in Fig. 1. It is because Rayleigh scattering plays a dominant role in the shorter wavelength (see Eq. (3)). The total radiance $L_t(\lambda)$ and the individual component of radiance

Table 1. Characteristics of the OSMI spectral bands.

Band No	B0	B1	B2	B3	B4	B5	Bx	B6
Center Wavelength(nm)	412	443	490	510	555	670	765	865
Bandwidth (nm)	20	20	20	20	20	20	40	40
SNR	350	450	450	450	350	350	350	350

Table 2. Simulation parameters of atmosphere, water, CET, and date.

Parameter		Values used	Notes
Date		Vernal Equinox, Summer Solstice Autumn Equinox, Winter Solstice	
CET		8:00 – 16:00 focus on 10:50	Sun glitter variation with CET; KOMPSAT design
Atmosphere	Pressure	1013.25 g/m^2	Standard air pressure
	Ozone	0.32 – 0.38 cm (NTP)	Typical air Iqbal, 1983
	Horizontal visibility	20 km (10 – 50 km)	Coast area to open sea
	Precipitation	2 cm (0.4 – 4 cm typically)	Coast area to open sea
	Wind speed	1.4-5m/s	Coast area to open sea
Water	Case I	Chlorophyll 0.5 mg/m^3 Suspended material 0.5 g/m^3 Yellow substance 0.001 mg/m^3 Ozone 0.32 cm (NTP) Wind speed 5 m/s	Open seawater
	Case II	Chlorophyll 5 mg/m^3 Suspended material 50 g/m^3 Yellow substance 0.5 mg/m^3 Ozone 0.36 cm (NTP) Wind speed 1.4 m/s	Coastal water

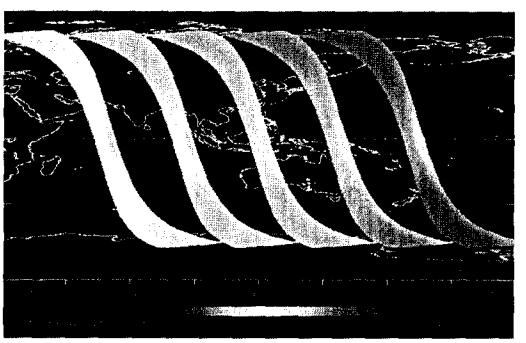

Fig. 1. Distributions of simulated total radiances for the OSMI spectral bands.

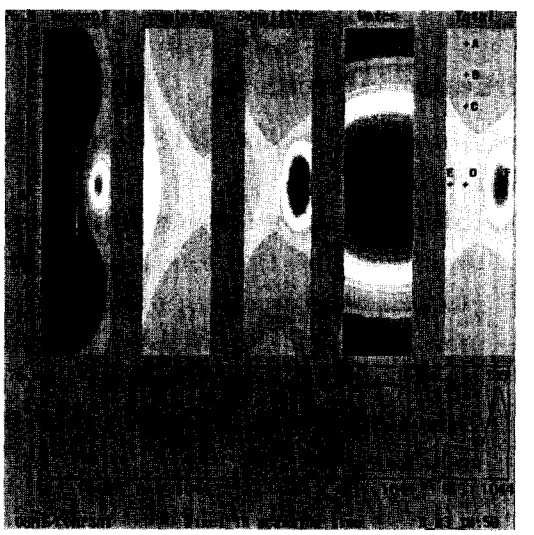

Fig. 2. Individual component of radiance for the OMSI band 3.

$[L_a(\lambda), L_r(\lambda), L_{sr}(\lambda), L_w(\lambda)]$ for six representative pixels (A, B, C, D, E, F in Fig. 2) have been calculated and illustrated in Fig. 2. The pixels A and B are at the high latitudes and C at the low latitudes but A and B at the same longitude. The D, E, F pixels are located near the equator. E represents the high Rayleigh scattering area, F for the sun glitter area and D between E and F. As for the total radiance, the band 1 value is about fifteen times as large as the band 6 counterpart except for

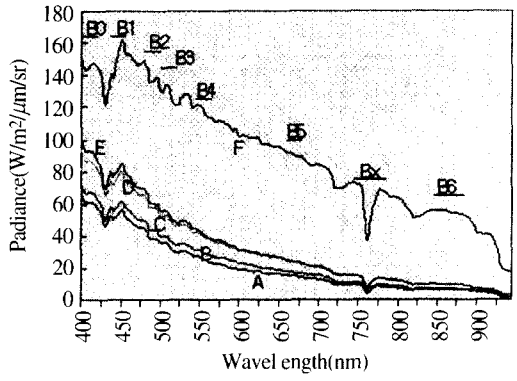

Fig. 3. Simulated spectral (total) radiances for the pixels as in Fig. 2.

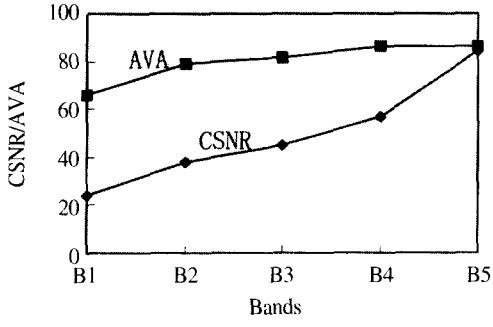

Fig. 5. CSNR and AVA averages of whole path image for the OSMI spectral bands.

the pixel F because of sun glitter.

The simulated spectral (total) radiances of six pixels are shown in Fig. 3. It is clear that the total radiance of all pixels in the image obviously decreases from band 1 to band 6.

Unlike the radiance variation with the wavelength, both CSNR and AVA increase with the wavelength. The series of CSNR image of different bands for the case I and case II water, and the average CSNR and AVA of whole orbit image show that the CSNR and AVA increase from band 1 to band 5. For example, the CSNR spatial distribution for case II water and the average CSNR and AVA of whole path image for the OSMI spectral bands are shown in Fig. 4 and

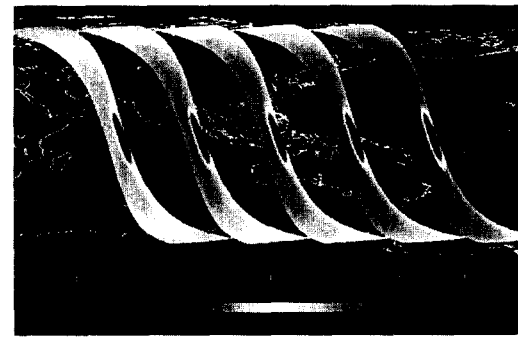

Fig. 4. CSNR patterns of case II water for the OSMI spectral bands.

Fig. 5, respectively. Both Fig. 4 and Fig. 5 also show that the band 5 for atmospheric correction with the assumption of zero radiance in clear water is efficient to measure the case II water because its CSNR and AVA are higher than other bands.

2) Image Properties at Different CET

The sun glitter will appear on the OSMI image because of its inability of tilt scanning. The distribution pattern of sun glitter depends on satellite orbit, sensor properties, wind speeds, CET and so forth, but is mainly decided by the CET if satellite orbit and sensor have been designed. To help understand how the sun glitter radiance pattern looks like and how it affects the CSNR and AVA in terms of the different CET, we select different bands to simulate the radiance image at different CETs (8:00, 9:00, 10:00, 11:00, 12:00, 13:00, 14:00, 15:00 and 16:00). Total radiance distributions of band 3 at different CETs from 8:00 to 16:00 are shown in Fig. 6. The followings are noticeable:

(a) The sun glitter starts to appear at CET 8:00, on the almost all of eastern edge of the image like a belt, but with weak reflection.

(b) When CET changes from 8:00 to 11:00, the sun glitter extends from eastern edge to the center

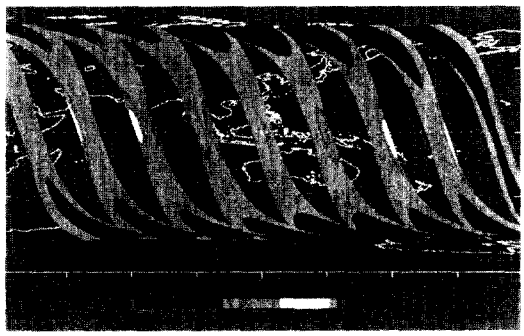

Fig. 6. Variation of total radiance (band 3) with CET.

of image. Its pattern varies from narrow belt (8:00), to small half of ellipse (9:00), to half of ellipse (10:00), and to whole ellipse (11:00). The highest radiance occurs at the center of sun glitter ellipse and gradually decreases from center to circumference.

(c) When CET close to 12:00 from 11:00, the sun glitter ellipse is shrinking to almost like a spot in the middle of image.

(d) When CET varies from 12:00 to 13:00, sun glitter ellipse appears again and moves to the western side of image.

(e) Finally, when CET changes from 13:00 to 16:00, the sun glitter ellipse varies from whole ellipse into a half ellipse (14:00 and 15:00), and into a belt pattern (16:00) on the western edge of the image, whose pattern is similar to the beginning of pattern (8:00) on the eastern edge.

To illustrate how strong the sun glitter is in the area of ellipse and how different from the non-sun glitter area under the OSMI sun-synchronous orbit of CET 10:50, we select the pixel F centered at the sun glitter ellipse and another pixel D from the non-sun glitter area (see Fig. 2). The spectra of different component radiances [$L_a(\lambda)$, $L_r(\lambda)$, $L_{sr}(\lambda)$, $L_w(\lambda)$ and $L_t(\lambda)$] of pixel F and pixel D are simulated and are shown in Fig. 7 and Fig. 8,

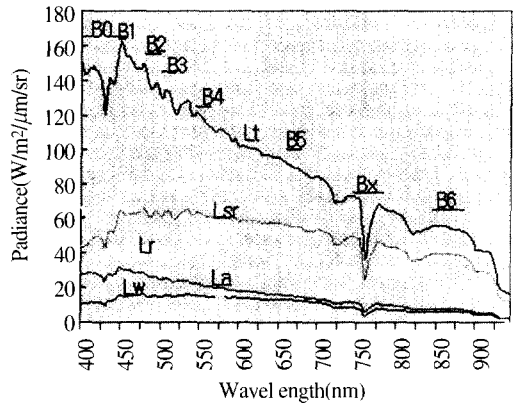

Fig. 7. Simulated radiance of each component for the pixel F located in the sun glitter area; case II water.

respectively. Comparing two figures, we can see the following features:

(a) The total radiance in the sun glitter area is almost 2 to 5 times stronger than the non-sun glitter area, and increases more in longer wavelength bands than shorter, mainly due to the sun glitter.

(b) The total radiance in the sun glitter area is dominated by sun glitter (see Fig. 7), but Rayleigh scattering is a major component in the non-sun glitter area (see Fig. 8).

(c) The sun glitter also causes the increase of aerosol scattering (see Fig. 8) because the sun glitter radiation is scattered by aerosol.

(d) Even though the very high sediment concentration in the case II water is applied to simulate the spectra in Fig. 7 and Fig. 8, the water leaving radiance is only about 7-12% of the total in the sun glitter area, but about 12-28% in the non-sun glitter area. When the case I water is applied, less water leaving radiance, only about 2.5-6% of the total in the sun glitter area and 8-15% in the non-sun glitter area. It indicates that atmospheric correction can be very difficult but should be made before the OSMI data is distributed to the user.

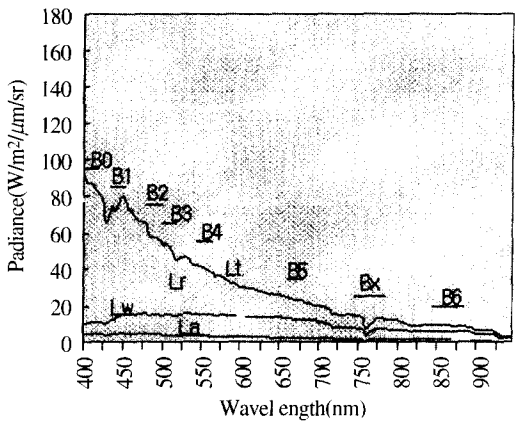

Fig. 8. Simulated radiance of each component for the pixel D located in the non-sun glitter area; case II water.

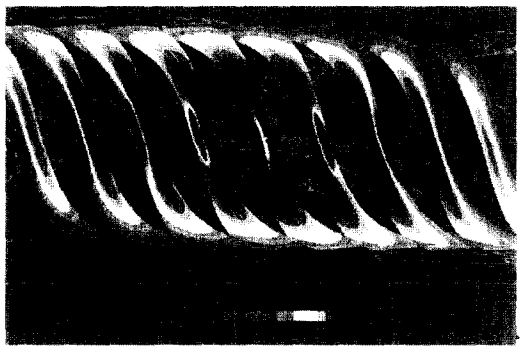

Fig. 9. Variation of CSNR (band 3) with CET.

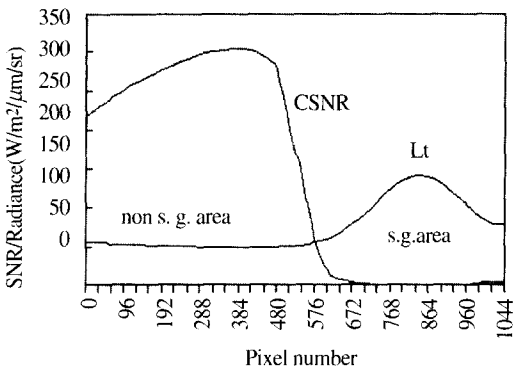

Fig. 10. Profiles of CSNR and total radiance of the scan line passing through the pixel D, E, and F.

To understand how CET affects the quality of OSMI image, a series of CSNR images have been simulated at different CETs from 8:00 to 16:00, as shown in Fig. 9. The CSNR patterns illustrate the followings:

(a) When CET is at 8:00, the CSNR values of whole image is the lowest compared to other CETs because of the lowest sun elevation in the early morning, but the distribution of CSNR looks much more homogenous than others.

(b) As CET varies from 8:00 to 12:00, CSNR generally increases except the ellipse area where sun glitter significantly affects. The best quality of image is at CET 12:00.

(c) When CET changes from 12:00 to 16:00, CSNR decreases and the distribution of CSNR image of CET 16:00 is quite similar to that of CET 8:00.

The CSNR image of OSMI would be like one at CET 11:00 in the Fig. 9. It is noted that the data quality of the eastern side of OSMI image is not satisfactory because of sun glitter (see Fig. 2, 4, 7, 8 and 11). To illustrate how the sun glitter affects CSNR, the profiles of CSNR and total radiance of the scan line passing through the pixel D, E, and F in Fig. 2 are plotted in Fig. 10. The total radiance received by satellite in the sun glitter area on the eastern side of OSMI image is much higher than in the non-sun glitter area, but much lower CSNR. Almost a half of line data is useless. Therefore, it is necessary to pay attention to the sun glitter problem in the OSMI image.

The averages of CSNR and AVA of whole orbit image for different visible bands are calculated by Eq. 47-50 at every half an hour from CET 8:00 to 16:00 for case I and case II water. Subsequently, the average for the spectral bands is taken and the results are shown in Fig. 11. It is obvious that both the average CSNR and AVA for case I or case II

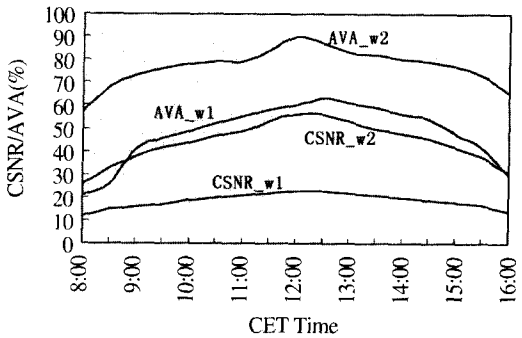

Fig. 11. Variation of the average CSNR and AVA of whole path image with CET; case I water (_w1), case II water (_w2).

water have the same distribution with the CET variation and that they would be better if they are closer to noon. Also we find that the case I water is more sensitive to the CET variation. The CSNR and AVA at CET 12:00 are 2 and 3 times respectively higher than at CET 8:00 for the case I water, but only about 2 to 1.5 times higher than for the case II water.

3) Evaluation Results

Since OSMI is designed to observe both global oceans and Korean seas, it would be interesting to compare the CSNR and AVA values between the whole orbit pass (global) and the Korean regional pass for four different seasons.

The simulated patterns of total radiance and CSNR for the OSMI band 3 are shown in Fig. 12. It is apparent that the location of sun glitter ellipse varies with seasons. The distributions of total radiance and CSNR in spring and autumn are more homogeneous and appear to be symmetric to the equator.

The images at high latitudes of the winter hemisphere are affected by lack of sunlight. The averages of CSNR and AVA for the 20800 scan lines of the whole orbit pass have been calculated for different seasons of case I and case II water

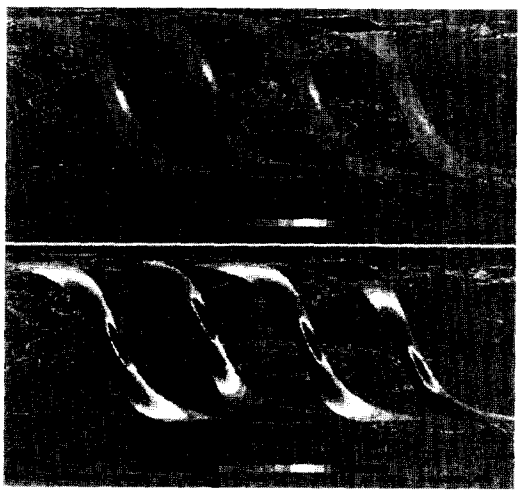

Fig. 12. Simulated image of the total radiance and CSNR (band 3) for four different seasons.

(Table 3). For both case I and case II water, the best seasons are autumn and spring. The worst season is summer for case I water and winter for case II water. In general, the availability of the OSMI image on a global scale is about 51% for case I water and 75% for case II water.

For the Korean region, we choose the image strip centered at 36.4°N and 128°E (5000 scan lines in an along-track). The CSNR patterns are not shown but the averages of CSNR and AVA are listed in Table 3. In general, the CSNR and AVA values of the Korean region are better than those of the whole orbit pass. Korea is located at fairly good latitudes under the given OSMI orbit. The annual availability of the OSMI image is about 65% for case I water and 88 % for case II water. The best season is spring for both case I and case II water. It is different from the whole orbit pass in that the good quality image could be obtained in winter. Because of the strong effect of sun glitter in summer, the worst quality image could be produced in this season.

In addition, the following points are notable from the comparison between global and regional

Table 3. Summary of the OSMI data evaluation.

	Global				Korean Region			
	Case I		Case II		Case I		Case II	
	CSNR	AVA	CSNR	AVA	CSNR	AVA	CSNR	AVA
Spring	20	54	48	79	28	82	50	100
Summer	18	46	47	74	16	39	44	63
Autumn	21	56	50	80	24	64	52	100
Winter	18	48	45	69	24	75	46	92
Average	19	51	47	75	23	65	48	88

* AVA with %

scale images:

(a) The image is more efficient in case II water than case I. The AVA is about 20% higher in case II water than case I.

(b) The AVA of image is more stable on a global scale than a regional scale.

(c) The AVA is higher in the Korean region compared to the whole orbit pass except for the summer.

(d) The image of the Korean region in summer will be seriously affected by sun glitter.

6. Conclusion

In this study, we have simulated the KOMPSAT/OSMI radiance imagery using the KOMPSAT orbit parameters and OSMI sensor characteristics for several cases of typical air-sea conditions. Simulation has been performed by models of geolocation and radiative transfer. Based on the simulated radiance imagery and the concept of CSNR, we have further attempted to evaluate the quality and availability of OSMI imagery. We summarize the findings in this study as follows:

- CSNR could serve as a reasonable index to evaluate the image data quality.
- The total radiance arrived at OSMI for case I and case II water decreases with the spectral wavelength. It is largely dominated by Rayleigh scatting in the most part of image, by aerosol scattering in the satellite nadir area, and by sun reflection in the sun glitter area. The eastern side of image is seriously degraded by sun glitter, especially in the summer of Korean region, where the water leaving radiance of case I water is only about 2.5-6% of total radiance.
- The OSMI data quality and availability depend on space and time. On a global scale, the best seasons for case I and case II water are spring and autumn. The worst season is summer for case I water, while winter being the worst for case II water. In general, the annual mean availability is about 50% for case I water and 75% for case II water. In the Korean region, the availability is higher than the global scale except for the summer when sun glitter seriously constrains the quality of image. The annual mean availability for case I water is about 65% and about 88% for case II water.

From the results of this study, the future work to improve the OSMI data quality, such as efforts for the data processing including atmospheric correction, the analysis of off-nadir observations over the Korean region, the comparison with SeaWiFS measurements in terms of the calibration and validation activity, is warranted.

Acknowledgments

This research was supported by the research grant (U98020-42-343) from the Korean Institute of Science Technology Evaluation and Policy (KISTEP). I (Delu Pan) am thankful for the arrangement of this program by Korea Aerospace Research Institute(KARI). Meanwhile, I would also thank the Satellite Avionics Department of KARI, especially the Data Receiving and Processing Team, for lots of kind help during this project. We also would like to thank reviewers for their valuable comments.

References

Andre, J.M. and A. Morel, 1989. Stimulated effects of barometric pressure and ozone content upon the estimate of marine phytoplankton from space, *J. Geophys. Res.*, 94 (c1) : 1029-1037.

Bricaud, A. and A. Morel, 1987. Atmospheric corrections and interpretation of marine radiances in CZCS imagery: use of a reflectance model, *Oceanol. Acta*, 7 : 33-50.

Cox, C. and W. Munk, 1954. Measurements of the roughness of the sea surface from photographs of the sun's glitter, *J. Opt. Soc. Am.*, 44 (11) : 838-850.

Doerffer, R., 1980. Application of a two-flow model for remote sensing of substances in water. *Boundary-Layer Meteorology*, 18 : 221-232.

Fischer, J., 1983. Fernenkundung von schwegbstoffen im Ozean, Hamburger Geophysikalische Einzelschriften, Herausg. von den Geophysikalischen Instituten der Universitat Hamburg, Reihe A, Heft 65.

Gordon, H.R. and D.J. Castano, 1989. Aerosol analysis with Coastal Zone Color Scanner: A simple method for including multiple scattering effects, *Applied Opt.*, Vol. 28, 1320-1326.

Gordon, H.R., 1990. Radiometric considerations for ocean color remote sensors, *Applied Opt.*, 29 : 3228-3236.

Hooker, S.B., W.E. Esaias, G.C. Feldman, W.W. Gregg, and C.R. McClain, 1992. An overview of SeaWiFS and ocean color, *NASA Tech. Memo. 104566, Vol. 1*, S.B. Hooker and E.R. Firestone, Eds., NASA Goddard Space Flight Center, Greenbelt, Maryland, 24 pp., plus color plates.

Iqbal, M., 1983. *An introduction to solar radiation*, Academic Press, Toronto, New York, London.

Paik, H. *et al.*, 1998. The KOMPSAT-1 payloads overview, Proc. of International Symposium on Remote Sensing, ISSN 1226-9743, 301-306.

Pan, D., R. Doerffer, T. Mao, and S. Li, 1996. A study of anchoring geographic coordinates and calculating zenith and azimuth of sun and scanner for oceanic satellite data, *Acta Oceanologica Sinica*, Vol.15, 539-557.

Pan D., R. Doerffer, T. Mao and S. Li, 1997. A simulation of radiation imagery for ocean color satellite, *Acta Ocanologica Sinica*, Vol.16, 171-191.

Sturm, B., 1981. The atmospheric correction of remotely sensed data and the quantitative determination of suspended matter in marine water surface layers, In Cracknell, A.P. (ed.), *Remote Sensing in Meteorology, Oceanography and Hydrology*, Chichester, Ellis Horwood, 163-197.